Supplementary Information for

Rapid recruitment of p53 to DNA damage sites directs DNA repair choice and integrity

YH Wang[†], TLF. Ho[†], A Hariharan, HC Goh, YL Wong, NS Verkaik, MY Lee, WL Tam, DC van Gent, AR Venkitaraman, MP Sheetz[*] and DP Lane[*]

MP Sheetz and DP Lane
Email: ms2001@columbia.edu and dplane@imcb.a-star.edu.sg

This PDF file includes:

> Figures S1 to S9
> Tables S1 and S2
> Legends for Movies S1 to S7

Other supplementary materials for this manuscript include the following:
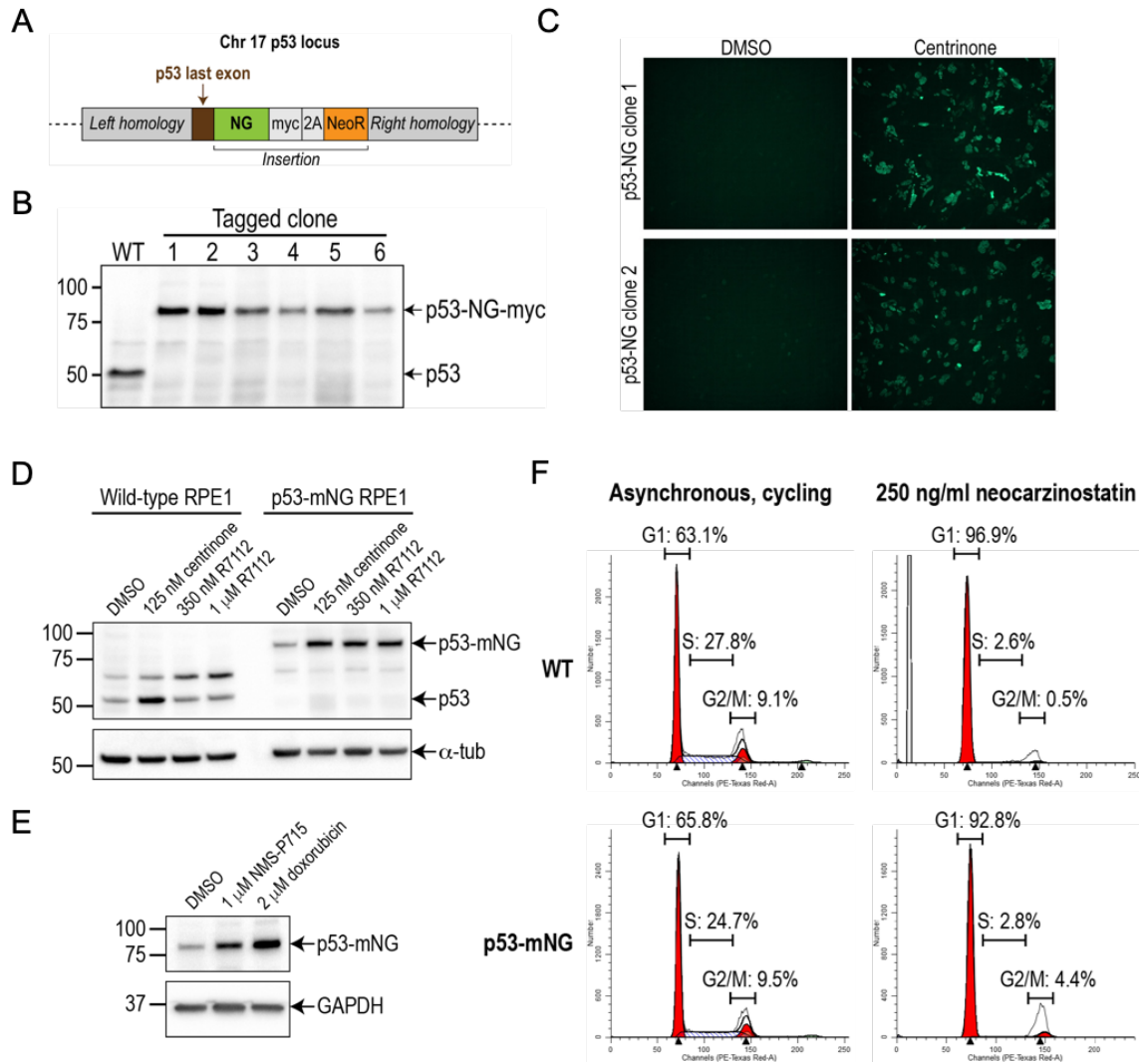
> Movies S1 to S7

Fig. S1. Generation of p53-mNG RPE1 cells using CRISPR. (**A**) Schematic representation of the design of homologous recombination template for introducing mNeonGreen at the C-terminal of endogenous p53 using CRISPR. (**B**) Single colony selection with successful biallelic labeling of p53 in RPE1 cells. (**C**) Fluorescent micrographs showing p53-mNG RPE1 cells upregulate p53 in response to a Plk4 inhibitor, centrinone, at 125 nM. (**D**) Western blots of lysates from wild-type and p53-mNG RPE1 cells treated with centrinone or the MDM2 inhibitor, R7112. P53-mNG resembled p53-wt and were upregulated in both cases. (**E**) Western blots of lysates from p53-mNG RPE1 cells showed upregulated p53-mNG levels upon treatment with MPS1 inhibitor NMS-P715 or the DNA damaging agent doxorubicin. (**F**) Cell cycle analysis following flow cytometry of propidium iodide-stained p53-mNG RPE1 cells. Both cell lines showed similar population in different cell cycle states under basal conditions. Like p53 WT cells, the p53-mNG cells mounted a G1 arrest response following treatment with the DNA damaging agent neocarzinostatin (NCS).
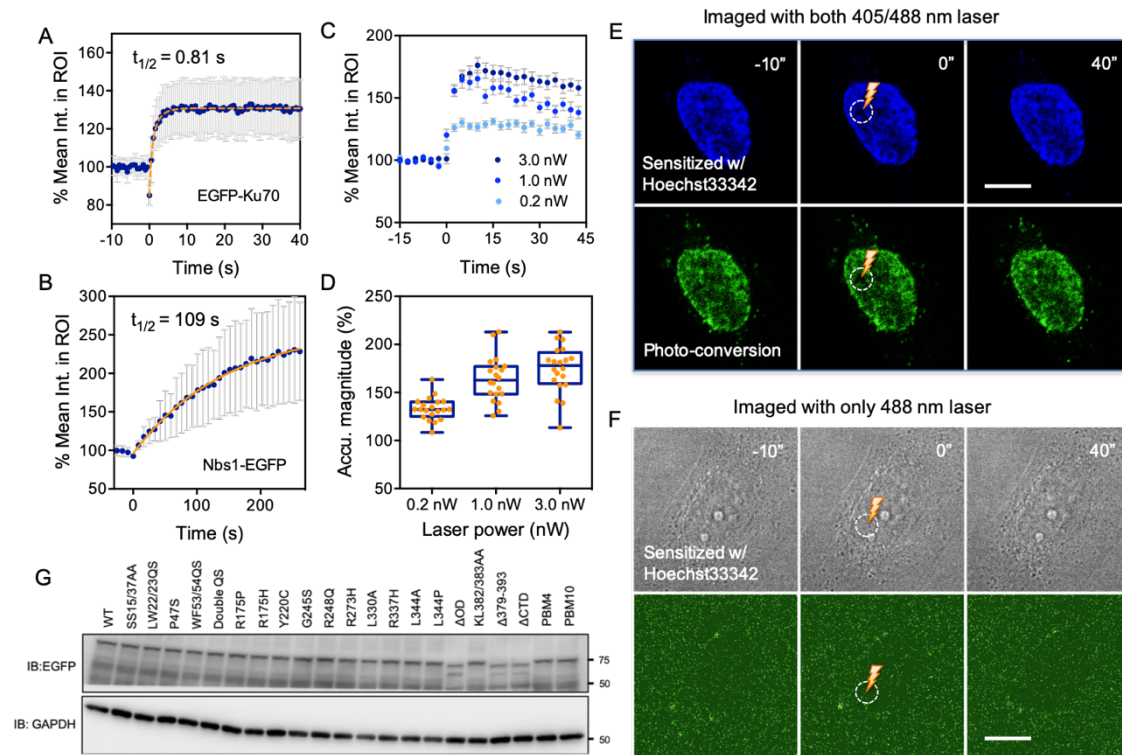
Fig. S2. Rapid accumulation of p53 was not due to Hoechst 33342 photo-conversion artifacts. (**A-B**) Time courses of fluorescence intensity within ROIs of (**A**) Ku70- and (**B**) Nbs1-EGFP fusion upon laser microirradiation with the same experimental settings used for p53. (**C**) Time courses of fluorescence intensity within ROIs of WT p53-EGFP in U2OS cells under different 355nm laser power with a constant exposure time of 500 ms. (mean±s.e.m., n= 20 for each condition) (**D**) Corresponding maximum magnitude of accumulation of WT p53-EGFP at different laser power. While the accumulation magnitude plateaued at about 3 nW, most experiments performed in this study has laser power set at 1 nW, as measured from the back aperture of the objective. (**E**) Non-transfected U2OS cells that are sensitized with Hoechst 33342 show global photo-conversion under the exposure of 405 nm laser. Local photo-conversion induced by a 355 nm laser at our experimental setting was not detectable. (**F**) Under the same condition, local photo-conversion induced by a 355 nm laser remains undetectable in the absence of global photo-conversion (by turning off the 405 nm laser). (G) The expression levels of exogenous WT and mutant p53-EGFP were relatively normalized by cell sorting of high intensity EGFP+ cells prior to analysis of transcriptional activity using a β−galactosidase assay, which corresponds to Figure 4E in the main text.
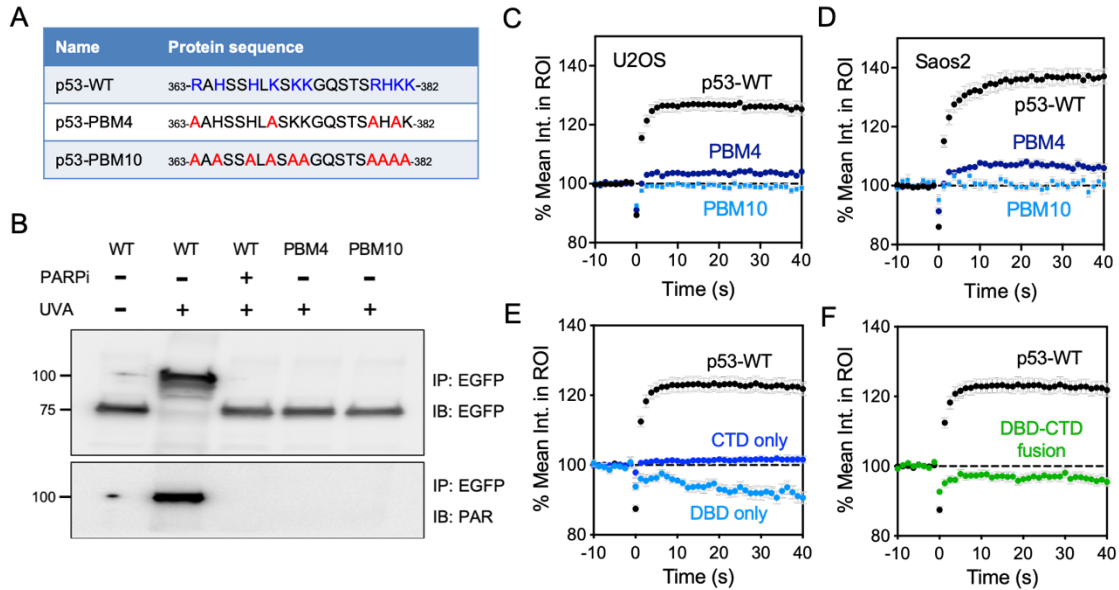
3

Fig. S3. Characterization of PARylation-deficient mutants of p53. (**A**) C-terminal domain sequences of p53 mutants, PBM4 and PBM10. (**B**) Immunoblotting of EGFP and PAR following immunoprecipiation with EGFP. PARPi (veliparib) suppressed UVA-induced PARylation of p53 in Saos2 cells. Unlike WT p53, PBM4 and PBM10 mutants were not PARylated after being exposed to UVA. (**C**) The lack of recruitment of both PBM4 (n=18) and PBM10 (n=13) mutants in comparison to the p53-WT (n=30) in U2OS, and (**D**) in Saos2 (PBM4, n=15; PBM10, n=14; p53-WT, n=20; mean±s.e.m.). (**E**) EGFP-tagged p53 DBD-only or CTD-only mutants were not able to rescue the phenotype (n= 19 & 20, respectively). (**F**) A mutant consisting of the DBD and CTD is not able to rescue the phenotype either in U2OS cells (mean±s.e.m., n= 15).
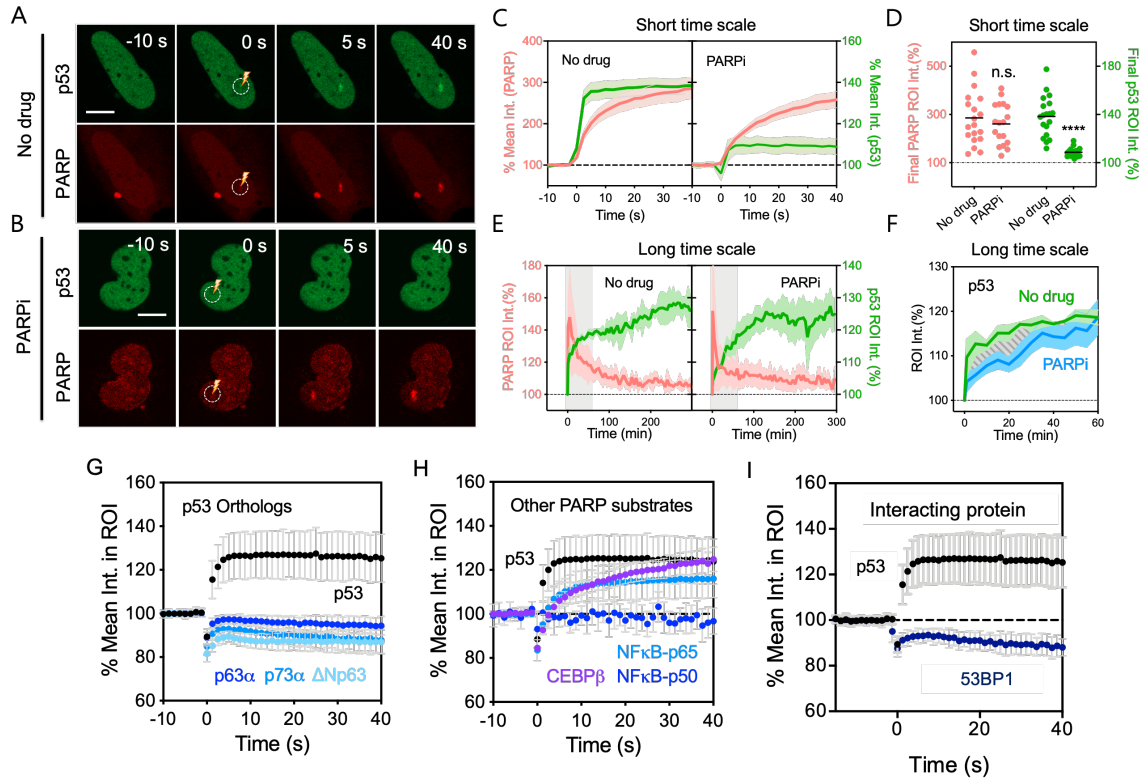
4

Fig. S4. PARP inhibitor suppresses early but not late recruitment of p53. (**A-B**) Representative montage showing recruitment of p53-EGFP and PARP-cb-RFP at shorter time scales (40 seconds) following laser microirradiation in the (**A**) absence and (**B**) presence of Veliparib in Saos2 cells. (**C**) Corresponding quantification of fluorescence intensity within ROI of WT p53-EGFP and PARP-cb-RFP over time (mean±s.e.m., n= 19 and 18, respectively.) (**D**) Normalized accumulation magnitudes of p53 and PARP at the end of the time course (t= 40 s) in panel **C**. (**E**) Quantification of wildtype (WT) p53-EGFP and PARP-cb-RFP intensities within ROIs in the absence and presence of Veliparib following laser microirradiation over a longer time scale (>300 minutes) (n=3). The shaded area is further examined in panel **F**. (**F**) The recruitment of p53 to damage sites is delayed in the presence of Veliparib by about an hour. (**G**) P63, p73 and their isoforms show no detectable accumulation at damage sites under the same experimental conditions. (**H**) Quantifications of fluorescence intensity changes within ROIs using other PARylation substrates: EGFP-tagged CEBPβ (n=14), NFκB p65 (n=24) and p50 (n=12) (mean±s.e.m.) (**I**) Quantifications of fluorescence intensity changes within ROIs of EGFP-tagged P53-binding protein 1 (53BP1) (n=12) (mean±s.e.m.).
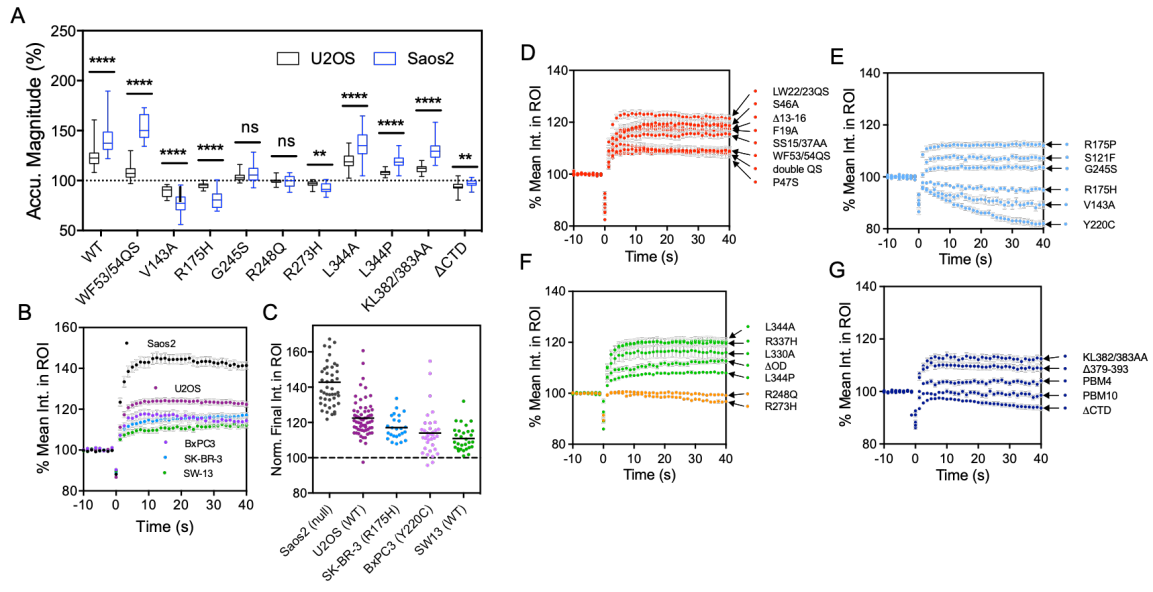
Fig. S5. Time course quantification of ROI fluorescence intensity in cells expressing WT and mutant p53-EGFP categorized by functional domains: (**A**) WT vs. ΔPRD mutants; (**B**) TAD mutants; (**C**) DBD contact mutants; (**D**) DBD conformational mutants; (**E**) CTD mutants; (**F**) OD mutants (mean±s.e.m., n= 15-54, N= 3). (**G**) Comparison of the magnitude of accumulation of WT and various mutant p53 when expressed in U2OS and Saos2 cells following irradiation (Box and whisker plot: Min to Max, n= 20-32, N= 3). (**H**) Time course quantification of the fluorescence intensity change within ROIs of WT p53-EGFP in different cancer cell lines carrying different p53 genetic background (mean±s.e.m., n= 19-48, N=3). (**I**) Corresponding quantification of p53 recruitment magnitude in each cell line at the end of the time course (t= 40 seconds).
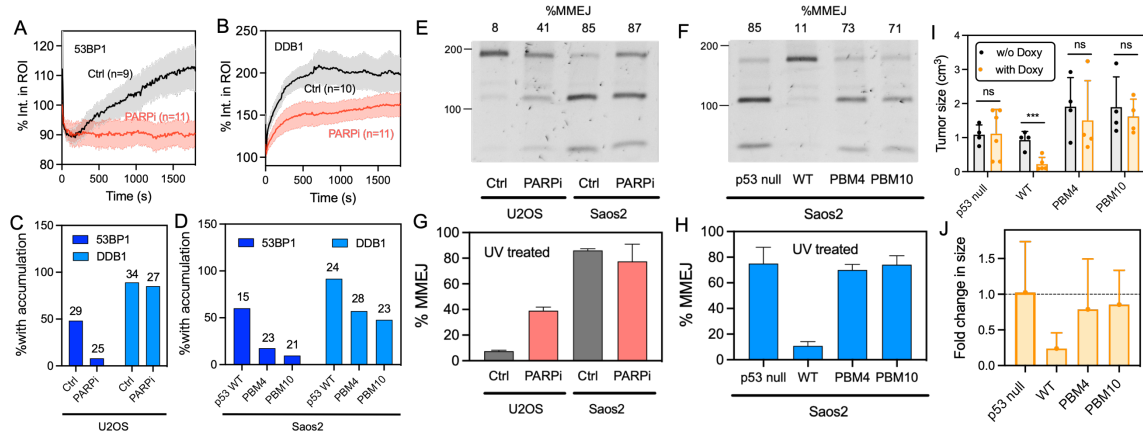
Fig. S6. Both PARP inhibitor and PARylation-deficient mutants suppress 53BP1 and DDB1 recruitment to DNA damage sites and favor MMEJ over NHEJ. (**A&B**) Temporal profiles showing that PARPi suppressed (**A**) 53BP1 and (**B**) DDB1 recruitment in laser microirradiation experiments (mean±s.e.m.). (**C**) Population fraction of cells showing 53BP1 and DDB1 recruitment in the presence and absence of PARPi following laser microirradiation in U2OS cells (p53 WT). Numbers on top of each bar represent sample numbers. (**D**) Population fraction of cells expressing PBM4 and PBM10 mutants showing 53BP1 and DDB1 recruitment in Saos2 cells (p53 null). Numbers on top of each bar represent sample numbers. (**E**) Electrophoresis of PCR products from an end-joining assay using UVA treated U2OS cells and Saos2 cell lines in the presence and absence of WT p53. (**F**) %MMEJ of Saos2 cells expressing WT, PBM4 or PBM10 mutant p53 in the same assay as described in (E). (**G&H**) Corresponding quantification of the ratio of band intensities in **E** and **F**, respectively (N=3 replicates, mean±s.d.). (**I**) Gross xenograft tumor of Saos2 cells with and without doxycycline-induced expression of p53 WT or PARylation mutants in immunocompromised NSG mice. Each dot represents an independent repeat (N≥2 mice, mean±s.d., ***p<0.005.) (**J**) Fold change in tumor volume with and without doxycycline induction. Error bars represent standard deviation that were calculated following error propagation principles.
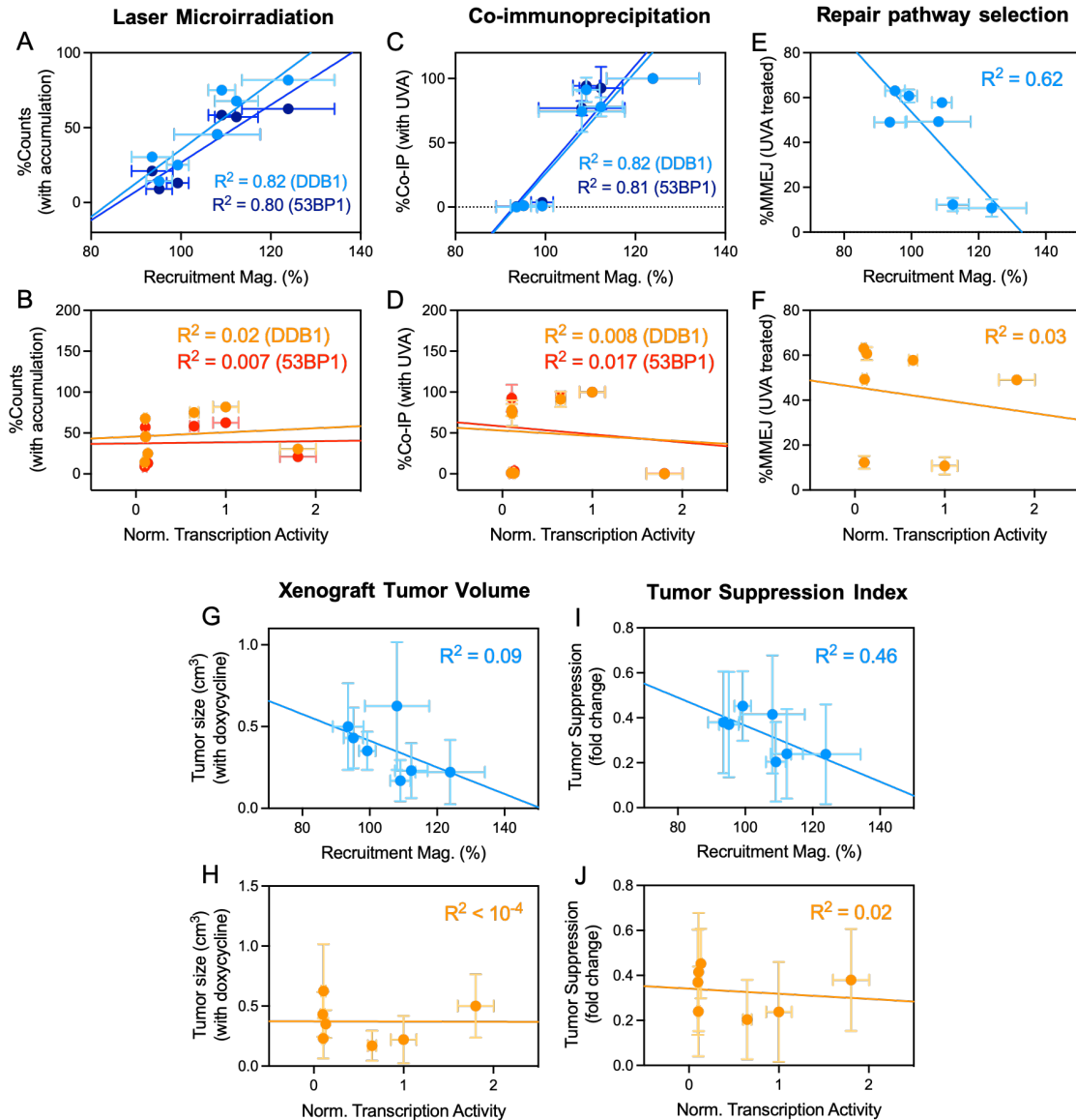
Fig. S7. Comparative correlation analyses reveal rapid recruitment, but not transcriptional activity, better correlates with protein interactions, repair pathway selection and tumor suppression. (**A&B**) Correlation between population fraction of cells with positive DDB1 or 53BP1 recruitment and rapid recruitment or normalized transcriptional activity of p53 following laser microirradiation. (**C&D**) Correlation between p53 co-immunoprecipitation with DDB1 or 53BP1 and rapid recruitment or normalized transcriptional activity of p53 shortly following UVA treatment. (**E&F**) Correlation between the %MMEJ from a plasmid recircularization assay and rapid recruitment or normalized transcriptional activity of p53 shortly following UVA treatment. (**G&H**) Correlation between the tumor volume with doxycycline induction of p53 expression and rapid recruitment or normalized transcriptional activity of p53. (**I&J**) Correlation between the fold change in tumor volume (with and without doxycycline induction of p53 expression) and rapid recruitment or normalized transcriptional activity of p53. (mean±s.d. for all panels)
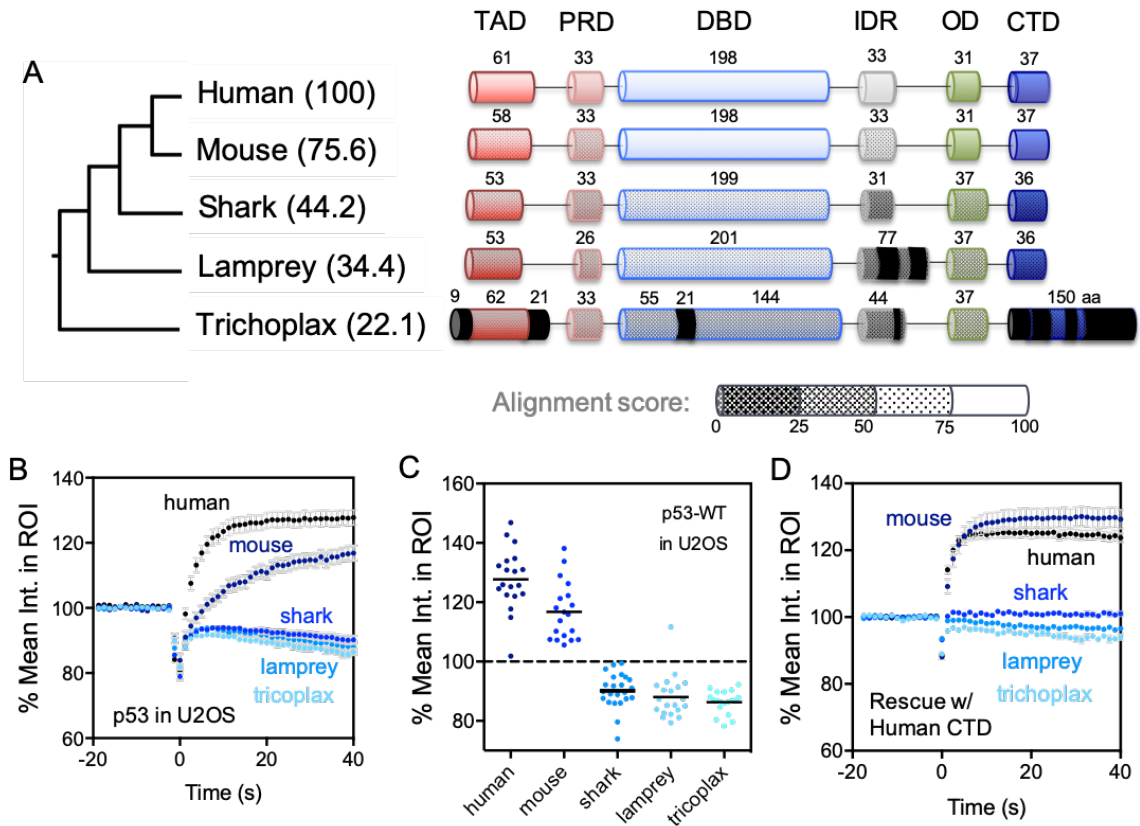
8

Fig. S8. Rapid recruitment of p53 is an acquired feature during evolution. (**A**) Phylogram of selected species-specific p53. Numbers in the parentheses indicate the scores of protein sequence alignment of the whole protein with respect to human p53. Structural homology is shown on the right with the size of each domain noted on top. Domains marked in black indicate additional sequences that cannot be aligned with human p53. Degrees of sequence homology of each domain with respect to those in human p53 are indicated by degrees of shading. (**B**) Time course of ROI fluorescent intensity show only human and murine p53 are rapidly recruited to damage sites in U2OS cells (n= 17-22, N= 3). (**C**) Accumulation magnitudes of different species-specific p53 at the end of the time course. (**D**) Chimera mutations of p53 from elephant shark, lamprey and trichoplax with their own CTD replaced by that from human p53 fail to rescue recruitment.
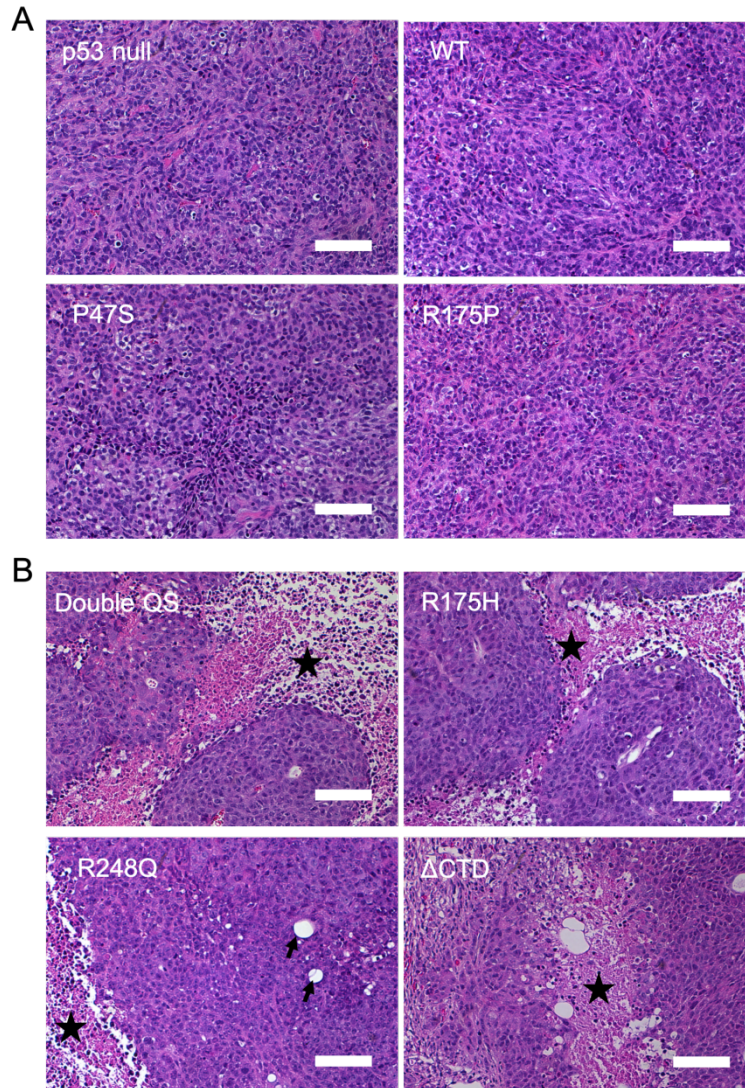
Fig. S9. Recruitment-competent and recruitment-deficient p53 mutants form tumors of differing sizes and degree of necrosis dependent on recruitment capability. Representative H&E stain images of sections derived from xenograft tumors arising from (**A**) p53-null Saos2 cells or Saos2 cells stably expressing WT or recruitment-competent p53 mutants; (**B**) Saos2 cells stably expressing recruitment-deficient p53 mutants. Stars denote areas of necrosis. Arrows denote regions of adipocyte infiltration (Scale bar = 100μm).

Table S1. Summary of domain-specific p53 mutants and recruitment to damage sites (Y: recruited; N: fail to be recruited; O: partially recruited).

P53 mutant	Domain targeted for mutation	Remarks	Transcription activity	Recruitment to damage	Tumor suppression in mouse models (PMID)
WT	—	Wildtype	Y	Y	Y (PMID 20452944)
Δ13-16	TAD	Hyperactive transactivation	O	Y	-
SS15/37AA	TAD	Phosphorylation mutant	O	Y	O (PMID 24415648)
LW22/23QS	TAD	Disrupt TAD I	O	Y	Y (PMID 27864306)
P47S	TAD	Disrupt TAD II	O	O	N (PMID 27034505)
WF53/54QS	TAD	Disrupt TAD II	N	O	Y (PMID 27864306)
Double QS	TAD	Disrupt both TAD I & II	N	O	N (PMID 27864306)
R175P	DBD	Conformational mutant	N	O	Y (PMID 14702042)
R175H	DBD	Conformational mutant	N	N	N (PMID 15607981)
Y220C	DBD	Conformational mutant	N	N	
G245S	DBD	Conformational mutant	N	N	N (PMID 23538418)
R248Q	DBD	DNA contact mutant	N	N	N (PMID 23538418)
R273H	DBD	DNA contact mutant	N	N	N (PMID 15607980)
L330A	OD	Monomer mutant	O	Y	-
L344A	OD	Dimer mutant	O	Y	-
L344P	OD	Monomer mutant	O	O	-
ΔOD	OD	Delete OD	N	O	-
KL382/383AA	CTD	Disrupt p53-CBP interaction	O	O	-
Δ379-393	CTD	Disrupt p53-PAR interaction	O	O	-
ΔCTD	CTD	Abolish p53-PAR interaction	Y	N	N (PMID 23770245)
PBM4	CTD	PARylation mutant	O	N	-
PBM10	CTD	PARylation mutant	O	N	-

Y: Yes   N: No   O: Partial

Table S2. Percentage of cells showing recruitment of various DDR proteins in the presence and absence of p53-wt. Proteins of interest are all major factors in their respective repair pathways. Number in the parentheses indicates total cells tested under given condition (N=3).

Table S2. Confirmed accumulation following damage within 30min		
DDR protein	**without p53**	**with p53-wt**
NER		
XPA	100 % (11)	100 % (10)
XPB	100 % (8)	100 % (8)
XPC	62.5 % (16)	73.3 % (15)
DDB1	25.0 % (16)	81.8 % (22)
NHEJ		
Ku70	81.3 % (16)	100 % (16)
XRCC4	80.0 % (10)	100 % (9)
53BP1	16.8 % (12)	62.5 % (16)
HR		
NBS1	100 % (11)	100 % (11)
Rad51	76.9 % (13)	92.9 % (14)
BRCA1	86.4 % (22)	100 % (16)

Supplementary Movies:

Movie S1. Rapid accumulation of endogenous p53-mNG in RPE1 cells.

Movie S2. Rapid accumulation of exogenously expressed wildtype p53-EGFP fusion protein in U2OS cells.

Movie S3. Lack of accumulation of exogenously expressed mutant p53 (R248Q-EGFP) fusion protein in U2OS cells.

Movie S4. Recruitment of wildtype p53-EGFP and PARP-cb-RFP fusion protein in Saos2 cells, in the absence (top panel) and presence (bottom panel) of PARP inhibitor.

Movie S5. P53-dependent recruitment of 53BP1 in Saos2 cells. Upper panel: 53BP1-EGFP alone. Lower panel: Co-transfection of 53BP1-EGFP and WT p53-mCherry.

Movie S6. P53-dependent recruitment of DDB1 in Saos2 cells. Upper panel: DDB1-EGFP alone. Lower panel: Co-transfection of DDB1-EGFP and WT p53-mCherry.

Movie S7. P53-independent recruitment of NBS1 in Saos2 cells. Upper panel: NBS1-EGFP alone. Lower panel: Co-transfection of NBS1-EGFP and WT p53-mCherry.